crystals

MDPI

Article

Wet Chemical Synthesis and Characterization of Au Coatings on Meso- and Macroporous Si for Molecular Analysis by SERS Spectroscopy

Siarhei Zavatski [1,2], Anatoli I. Popov [3,4,*], Andrey Chemenev [1], Alma Dauletbekova [4] and Hanna Bandarenka [1,2,*]

[1] Applied Plasmonics Laboratory, Belarusian State University of Informatics and Radioelectronics, 220013 Minsk, Belarus
[2] Institute of Advanced Materials and Technologies, National Research University of Electronic Technology, 124498 Zelenograd, Russia
[3] Institute of Solid State Physics, University of Latvia, LV-1063 Riga, Latvia
[4] Department of Technical Physics, L.N. Gumilyov Eurasian National University, Astana 010008, Kazakhstan
* Correspondence: popov@latnet.lv (A.I.P.); h.bandarenka@bsuir.by (H.B.)

Abstract: Porous silicon (PS) is a promising material for nanostructure fabrication providing a precise control over its size, shape, and spatial distribution. This makes it an excellent candidate for constructing highly sensitive, reproducible, and low-cost platforms for surface enhanced Raman scattering (SERS) spectroscopy. In this work, we connect the PS structural parameters with the morphology of the gold nanostructures fabricated on its surface, placing the emphasis on the SERS response. Two different types of PS are considered here, namely meso- and macro-PS. The former is prepared by Si electrochemical etching, applying three different current densities: 100 mA cm^{-2}, 60 mA cm^{-2}, and 30 mA cm^{-2}, while the technological parameters for the latter are selected to mimic metal nanovoids' (Me NVs) configuration. The gold-coated PS surfaces are produced via an electroless chemical deposition method for different time periods. By performing comprehensive structural, morphological, and optical characterization, we show the importance of the size and density of the PS pore openings, which govern the Au growth kinetics. The results presented in this work assure a simple yet flexible approach for the fabrication of large-area plasmonic gold nanostructures, which are not only suitable for advanced SERS spectroscopy studies but can also serve for a wider range of plasmonic applications.

Keywords: porous silicon; gold; fabrication; SERS; XRD

Citation: Zavatski, S.; Popov, A.I.; Chemenev, A.; Dauletbekova, A.; Bandarenka, H. Wet Chemical Synthesis and Characterization of Au Coatings on Meso- and Macroporous Si for Molecular Analysis by SERS Spectroscopy. *Crystals* **2022**, *12*, 1656. https://doi.org/10.3390/cryst12111656

Academic Editor: George D. Verros

Received: 30 October 2022
Accepted: 14 November 2022
Published: 17 November 2022

Publisher's Note: MDPI stays neutral with regard to jurisdictional claims in published maps and institutional affiliations.

1. Introduction

Nowadays, the rapid development of biomedicine has been increasingly faced with a demand for the detection, identification, and structural study of different organic analytes in trace amounts. Several sensing techniques, such as X-ray crystallography [1], nuclear magnetic resonance [2,3], and circular dichroism spectroscopy [4], have been applied to meet these needs. However, their routine application outside the framework of laboratory usage remains challenging: the low speed, high cost, complexity, and lack of complete databases [5] are major limitations for their practical implementation.

On the other hand, vibrational spectroscopy is a well-established molecular characterization technique [6], which does not require complex sample preparation and is widely used to study organic substances, e.g., in medicine [7], biology [8,9], the food industry [10], and pharmaceutics [11–13], to name a few. Utilizing the latest advancements of the Surface Enhanced Raman Scattering (SERS) spectroscopy technique, it is also possible to perform the detailed structure assignment of intricate substances, such as peptides, in small concentrations [14]. This is because of the extremely high sensitivity of the SERS technique

along with the ability to provide molecule fingerprints [15,16]. In addition, the analysis procedure with SERS spectroscopy is currently straightforward, making it a solid candidate for future sensing techniques in a wide range of applications.

The SERS effect is associated with a local electromagnetic field enhancement in the vicinity of the metallic nanostructure as the result of the resonance light interaction with localized surface plasmons (LSP) [17–19]. The magnitude of this enhancement is defined by the material choice (usually one of the coinage metals), size, and shape of the nanostructure. Hence, the research directed towards maximizing the local electromagnetic fields of a nanoscale platform is of particular importance for SERS sensing. From a practical point of view, however, such a platform must also demonstrate remarkable spot-to-spot and sample-to-sample SERS signal reproducibility, preserve the stability of the signal intensity over the long storage time, and offer inexpensive large-scale production [20]. In attempts to meet these strict requirements, several types of SERS substrates have been already developed, including colloidal solutions of metallic nanoparticles [16,21] and solid-supported arrays of metallic nanostructures with different shapes [22–25]. Although colloids usually exhibit high enhancement factors [16,26], solid metallic nanostructures are more convenient for utilization and demonstrate better signal reproducibility. Nevertheless, existing commercially available solid SERS platforms are produced via multistage nanoengineering processes, which inevitably increases their fabrication cost [27–31]. Therefore, exploring other possible SERS platform fabrication strategies remains a crucial task for ensuring broader SERS spectroscopy implementation in practice.

One such promising strategy is the utilization of matrices based on porous silicon (PS) to create the metal nanostructures on their surfaces [32,33]. PS represents a net of the periodically altered pore channels formed in Si. It has recently enabled an accurate control over the morphology of deposited silver layers, leading to a considerable improvement in SERS signal reproducibility [34,35]. The extraordinary detection limit down to the attomolar concentration of lactoferrin protein adsorbed on silvered meso-PS covered with graphene has been also demonstrated [9]. The macroporous PS on the other hand has facilitated the formation of such sophisticated structures as nanothorns, nanospongy films, dendrites, and many others [36–38], reaching the prominent 10^{-11}–10^{-15} M detection limit range. Owing to the PS capability to precisely control the nanostructures' morphology, its utilization for SERS has attracted extensive research during the past decade. The major advantages and unveiled limitations of metal-coated PS SERS platforms have been comprehensively discussed in several recent review articles [39,40].

Even though many studies have highlighted the effectiveness of PS-based SERS platforms, most of them are associated with silver nanostructures, which display several critical drawbacks, while utilizing SERS, especially when studying biomolecules. One familiar issue that the LSP resonance band for the silver nanoparticles lies in the range of 370–500 nm, depending on the size of the nanoparticles. Hence, to achieve the optimum resonance conditions and thus the maximum SERS response, the LSP energy must closely match with the excitation laser energy. Therefore, the usage of high-energy (small wavelength) laser excitations is usually required in experiments. This excitation is destructive for the majority of organic analytes. Moreover, considering that silver itself exhibits antibacterial activity [41,42], the resulting SERS spectra intensities may be dramatically decreased. The solution for these is relatively simple: silver can be replaced with gold, but this has rarely been performed for the metalized PS platforms.

In this work, we therefore propose to replace the silver coverage with a more stable and biocompatible gold layer to develop an effective SERS platform based on PS, and we also fill the existing gap in the studies of gold deposition mechanisms on different types of PS.

2. Materials and Methods

2.1. PS Substrate Fabrication

The PS was fabricated by the electrochemical anodic etching of a monocrystalline silicon wafer with (100) surface crystallographic orientation, according to the procedure

described elsewhere [43]. Briefly, an n^+- and p^--Si wafer was used to grow meso- and macro-PS, respectively. Just before anodization, the native silicon dioxide was removed from a silicon sample by etching in a diluted hydrofluoric acid (4.5%) for 60 s. After that, the Si sample was placed in a horizontal electrolytic cell made of polytetrafluoroethylene. An aqueous–alcoholic solution made of HF (45%), deionized water, and isopropanol at a volume ratio of 1:3:1 was used to prepare the meso-PS. Dimethylsulfoxide (DMSO) mixed with HF (45%) at the volume ratio of 10:46 was used for the macro-PS fabrication. The prepared solutions were gently added to the electrolytic cell. The meso-PS samples were fabricated at 100 mA cm^{-2}, 60 mA cm^{-2}, and 30 mA cm^{-2} current densities applied for 20 s, 22 s, and 20 s, respectively. The macro-PS samples were produced at an 8 mA cm^{-2} current density applied for 4 min. All freshly prepared PS samples were rinsed with deionized water and air dried.

2.2. Gold Deposition and Samples' Characterization

Gold was deposited by the immersion of a PS sample in an aqueous solution of 0.01 M $KAu(CN)_2$ and 0.15 M HF for different time periods according to the slightly changed procedure reported before [44]. Subsequently, freshly prepared samples were carefully washed with deionized water and air dried.

The organic dye rhodamine 6G (R6G) was used as an analyte for the SERS study. The dye molecules were adsorbed on the gold-coated PS sample by dipping it in a 10^{-6} M aqueous solution for 2 h. Each substrate was then thoroughly rinsed with deionized water for 30 s to remove the excess analyte molecules.

The morphology of the gold-coated PS was studied by scanning electron microscopy (SEM) with the help of an FESEM Hitachi−S4800 microscope. The crystallinity of the samples was studied with X-ray diffraction (XRD) using Cu K_α radiation (X-ray wavelength $\lambda = 0.15406$ nm). The SEM images were analyzed using ImageJ software. Reflectance spectra measurements were performed in the 350–900 nm wavelength range with the help of a Shimadzu UV-3600 equipped with an integrating sphere module (ISR-2200). SERS spectra were acquired with the help of a WITec Scanning Near-field Optical Microscope alpha300 S equipped with a 532 nm laser diode and an 60x air objective (0.9 NA). The spectra were acquired with 1 mW laser power for 1 s sample surface exposition.

3. Results and Discussion

3.1. Morphology of the Au-Coated Meso-PS Substrates

The electroless (galvanic, corrosion) deposition of the Au films on monocrystalline Si surfaces followed the oxidation–reduction (redox) mechanism, which assumes the reduction of Au^{3+} cations to atomic Au^0 by electron (e^-) exchange with Si. It is known that the redox potential for Au^{3+}/Au^0 is positive in the presence of Si atoms [45]. Hence, the Au deposition proceeded spontaneously as the result of the electron transfer from semiconductor valence band to metal cations:

$$Au^{3+} + 3e^- \rightarrow Au^0. \quad (1)$$

As the result of this process, the Si was simultaneously oxidized, since the above reduction reaction can be also viewed in terms of the holes (h^+) "injection" into the valence band of Si. This injection in the presence of H_2O induced silicon dioxide formation:

$$Si + H_2O + 4h^+ \rightarrow SiO_2 + 4H^+. \quad (2)$$

On a large timescale, the gold deposition is limited by the passivation of the Si surface with the oxide, reducing the process rate. However, with the presence of HF in the solution, the SiO_2 can be dissolved, producing new charge carriers and water soluble SiF_6^{2-} species:

$$SiO_2 + 6HF \rightarrow SiF_6^{2-} + 2H^+ + 2H_2O. \quad (3)$$

In these conditions, the Au electroless deposition on the Si is not limited by SiO_2 growth, and new Au nuclei form on the already adsorbed metal clusters and the available Si surface. Notably, the former is possible due to the galvanic cell formation between the noble metals and Si [46].

Considering a porous instead of monocrystalline Si surface, an important role for Au deposition is the presence of Si-H_x groups, which are usually generated via the hydration of uncompensated Si bonds produced upon electrochemical Si etching. These hydrated bonds are very reactive and can be easily oxidized, releasing additional electrons, and thus accelerating Au deposition:

$$2Si–H_{x(surface)} + H_2O \rightarrow SiO_{2(surface)} + 2H^+ + 4e^-. \quad (4)$$

Therefore, porous Si substrates can act not only as shape-forming platforms for plasmonic nanostructures due to the diversity of their surface configurations (meso-, macro-, and microporous surfaces of different porosity), but they also can control the redox reaction kinetics, which is an intriguing approach for producing even more sophisticated nanostructures, such as noble metal dendrites [47] or nanothorns [37].

Figure 1 shows the SEM images for the meso-PS templates prepared by different electrochemical etching regimes. Figure 1a reports a meso-PS etched at 30 mA cm^{-2} for 20 s, while Figure 1b,c show samples etched at 60 mA cm^{-2} and 100 mA cm^{-2} for 22 s and 20 s, respectively. Figure 1 confirms the PS formation with round pore openings of different sizes and densities. In all cases, a 1.3 μm thick PS layer was produced.

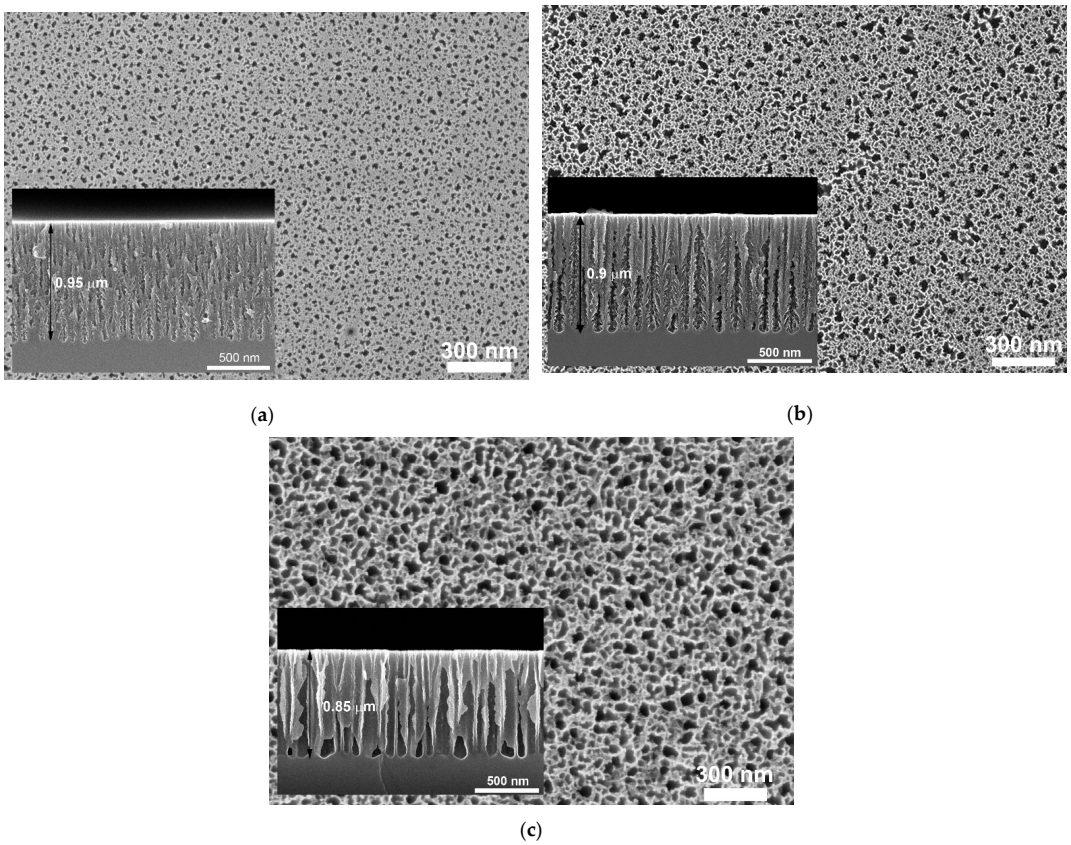

Figure 1. SEM images for a meso-PS sample after etching at a (**a**) 30 mA cm^{-2}, (**b**) 60 mA cm^{-2}, and (**c**) 100 mA cm^{-2} current density. The top views are presented in the background, while the cross sections are in the insets.

The quantitative characterization of the PS was carried out with the calculation of the mean pore opening diameter, pore density, and porosity. The mean pore diameter was calculated by averaging a Feret diameter distribution [48]. The pore density was calculated by dividing the number of pore openings by the visible surface area. The porosity of the

meso-PS samples was estimated by gravimetric [49] and SEM image assessment methods. Both approaches resulted in the same porosities. When the applied etching current density was 30 mA cm^{-2}, we obtained an average pore diameter of 19 nm ± 8 nm, a pore density of 5.3 × 10^{10} cm^{-2}, and 49% porosity. For the sample etched at 60 mA cm^{-2}, we obtained an average pore diameter of 28 nm ± 14 nm, a pore density of 3.1 × 10^{10} cm^{-2}, and 59% porosity. For the highest etching current density of 100 mA cm^{-2}, we obtained an average pore diameter of 44 nm ± 32 nm, a pore density of 2.8 × 10^{10} cm^{-2}, and 72% porosity. These data are in good agreement with the well-studied mechanism of PS formation [50,51] and reported experimental observations [52,53], albeit the density of the pores slightly decreased for the more porous samples. Based on the obtained results, we can attribute the fabricated samples to the mesoporous material [54].

The fabricated meso-PS matrices were utilized for the following gold deposition step. Figure 2 represents the SEM images for different Au-coated meso-PS substrates. The first row shows the samples obtained after 30 min of Au deposition, while the second row represents the samples after 70 min of Au deposition. Each column in the figure corresponds to the gold nanostructure on the meso-PS etched at different current densities: 30 mA cm^{-2}, 60 mA cm^{-2}, and 100 mA cm^{-2}. The increase in the Au deposition time led to the gold layer densification, producing a void-free continuous film along with a second Au layer nucleation (observe the material excess on top of the formed layer in Figure 2a,d). The same morphology evolution of a gold layer was obtained when the porosity of the PS was reduced, while keeping the Au deposition time constant (Figure 2a–c). Notably, no significant layer alteration was revealed when the porosity of PS varied at higher Au deposition times (Figure 2d–f). The analysis of the SEM images indicated that the gold coverage level increased from ~83% to ~97% after 30 min and 70 min of Au deposition, respectively, and did not alter significantly for different PS matrixes. Although the produced gold coverage represented a rather quasicontinuous film, there was still a meaningful number of Au nanoparticles (NPs). Hence, we estimated their mean diameter and standard deviation, which were varied within the 22–60 nm range for PS matrices after 30 min Au deposition, while the 70 min Au deposition produced 31–46 nm NPs (Figure 3).

These results reveal the importance of the meso-PS matrix morphology for the accurate control over the Au layer fabrication process. The obtained Au layer was defined by a PS surface, which contained an array of densely packed voids on the silicon surface (Figure 1a–c). Their density primarily depended on the etching current density and could be characterized by the porosity of the PS. As a rule, the higher the porosity, the denser the void package on the surface, and the lower the "free" silicon area. Consequently, the gold deposition rate, which followed the redox reaction mechanism between the silicon atoms and gold cations, was dramatically reduced for the highly porous matrices. The number of seed nucleation centers, as well as the surface diffusion of the gold atoms, were restricted by the voids, preventing the growth of a continuous Au film. Therefore, the Au coverage appeared in the form of isolated islands, whose sizes strongly depended on the porosity of the parent meso-PS matrix. It should be emphasized, however, that the situation changed in the later stages of Au film growth (Figure 2d–f). In these stages, the produced Au nanoislands became new nucleation centers, leading to the film growth over the pore openings. Eventually, the Au nanoislands collapsed, and the quasicontinuous Au film on top of the porous surface was achieved. Continuing the Au deposition induced the new Au layer formation. Interestingly, the appearance of this layer started with NP nucleation, suggesting that the Au film formation followed the Stranski–Krastanov mechanism of thin films' growth [55–57].

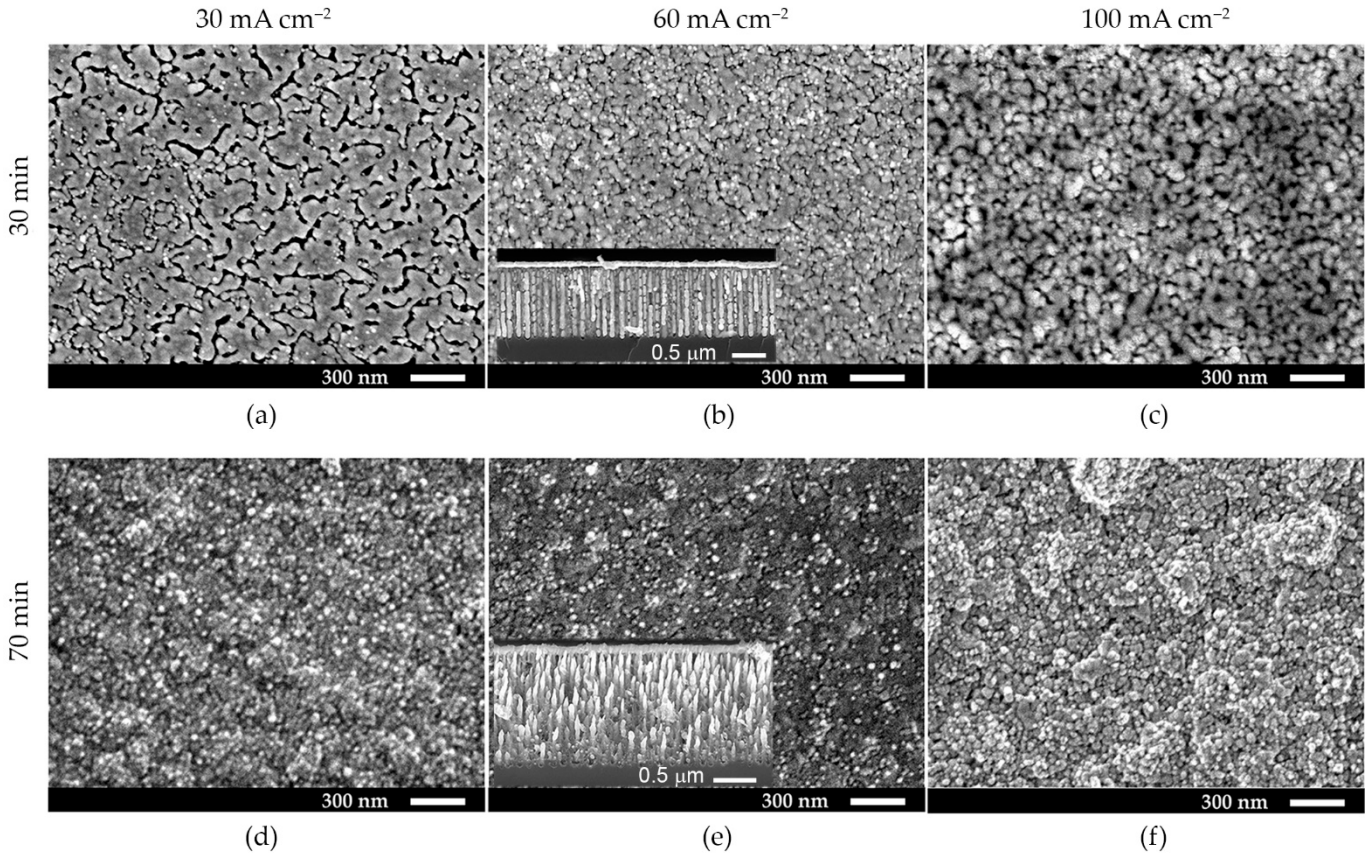

Figure 2. SEM images after Au deposition on the PS with a 49% (**a**,**d**), 59% (**b**,**e**), and 72% (**c**,**f**) porosity for 30 min (**a**–**c**) and 70 min (**d**–**f**). The insets in (**b**,**e**) depict the cross-section view for the meso-PS after the Au deposition.

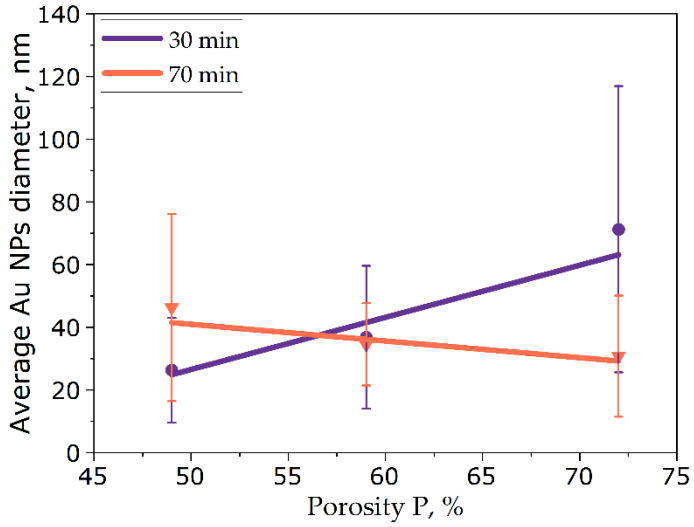

Figure 3. Evolution of the mean Au NP diameter as a function of the meso-PS porosity for different gold deposition times.

Figure 4 reports the XRD pattern for the Au-coated meso-PS after 30 min and 70 min of Au deposition on the PS etched at 60 mA cm^{-2}. As can be seen from Figure 4, both XRD patterns contained the characteristic peaks for the cubic cell Au crystals with orientations (111), (200), (220), and (311), confirming the polycrystalline nature of the Au coverage. Remarkably, the intensity of the (200) peak increased after 70 min of Au deposition, while

the other peaks became less prominent, compare Figure 4a,b. These data indicate the gold coverage growth along with the deformation of a Au elementary crystal cell by a Si surface with (100) crystallographic orientation, leading to the monocrystallization of the Au coverage. The appearance of the Si (400) peak, however, suggested a weak uniformity of the Au layer for both samples. The same XRD patterns were observed for all the Au-coated meso-PS samples, albeit with a minor intensity variation of the characteristic peaks, depending on the porosity of the meso-PS and the Au deposition time.

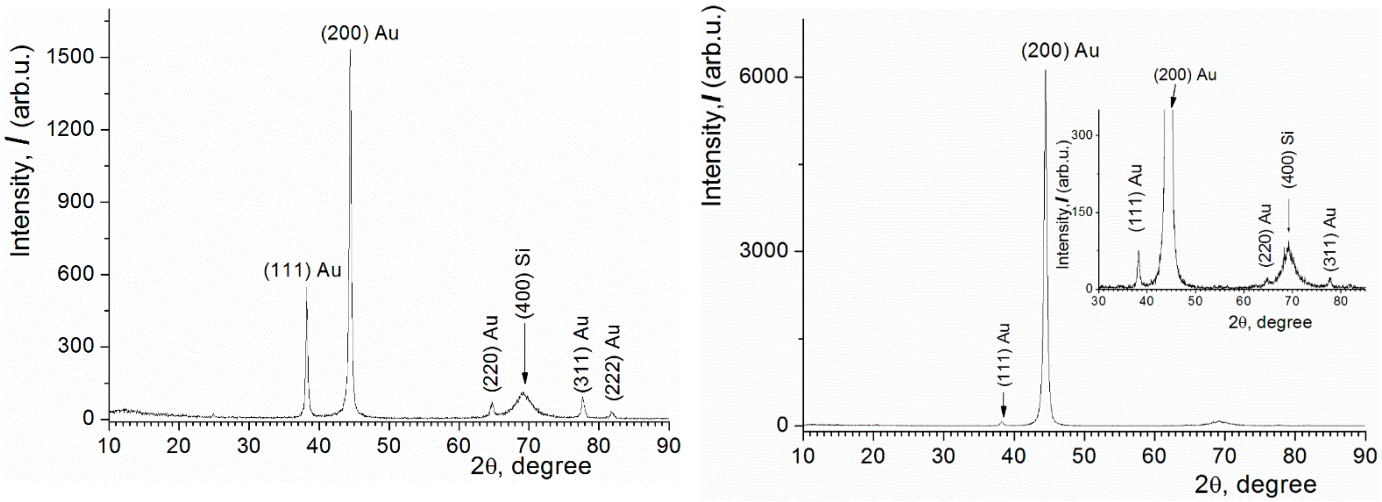

Figure 4. XRD pattern after 30 min (**a**) and 70 min (**b**) of Au deposition on the meso-PS with 49% porosity.

3.2. Morphology of the Au-Coated Macro-PS Substrates

Figure 5 reports the SEM images for the macro-PS template and the corresponding distribution of the pore openings' diameter. The SEM images confirmed the 1.1 µm thick PS layer formation with round pore openings (Figure 5a). The pore diameters' distribution for the macro-PS was rather nonuniform, covering the 400–1000 nm range (Figure 5b). These sizes were about one order of magnitude larger compared to the meso-PS (Figure 1). We therefore attributed the obtained sample to the macroporous material [54]. These results were in good agreement with the established macro-PS formation models [51].

Figure 6 shows the SEM images for the Au-coated macro-PS substrates after 30–80 min of Au deposition. The morphology of the film altered dramatically at various Au deposition steps. An array of closely packed Au NPs was obtained after 30 min deposition, Figure 6a. These NPs coalesced after 40 min producing a quasicontinuous gold film, as shown in Figure 6b. The subsequent increase in the deposition time led to the film densification together with the new Au seeds' nucleation over the formed coverage, producing a multilayered Au film, as shown in Figure 6c–f. The analysis of the SEM images depicted in Figure 7 reported the average Au NP diameter after different deposition times. No noticeable dependence of NP size on the deposition time was observed. The average Au NP diameter for all samples varied from 50 nm to 60 nm. The statistical data for the samples after 30 min and 40 min of Au deposition is not reported due to the difficulties in distinguishing individual Au NPs.

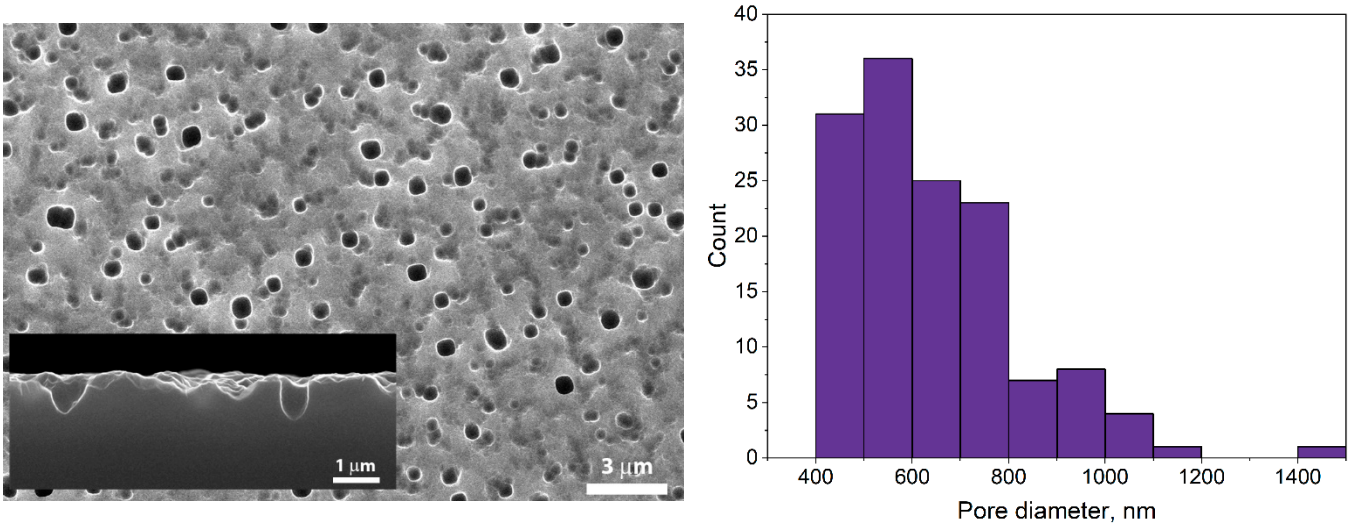

(**a**) (**b**)

Figure 5. SEM images for a macro-PS sample (**a**) and the corresponding distribution of the pore opening diameters (**b**).

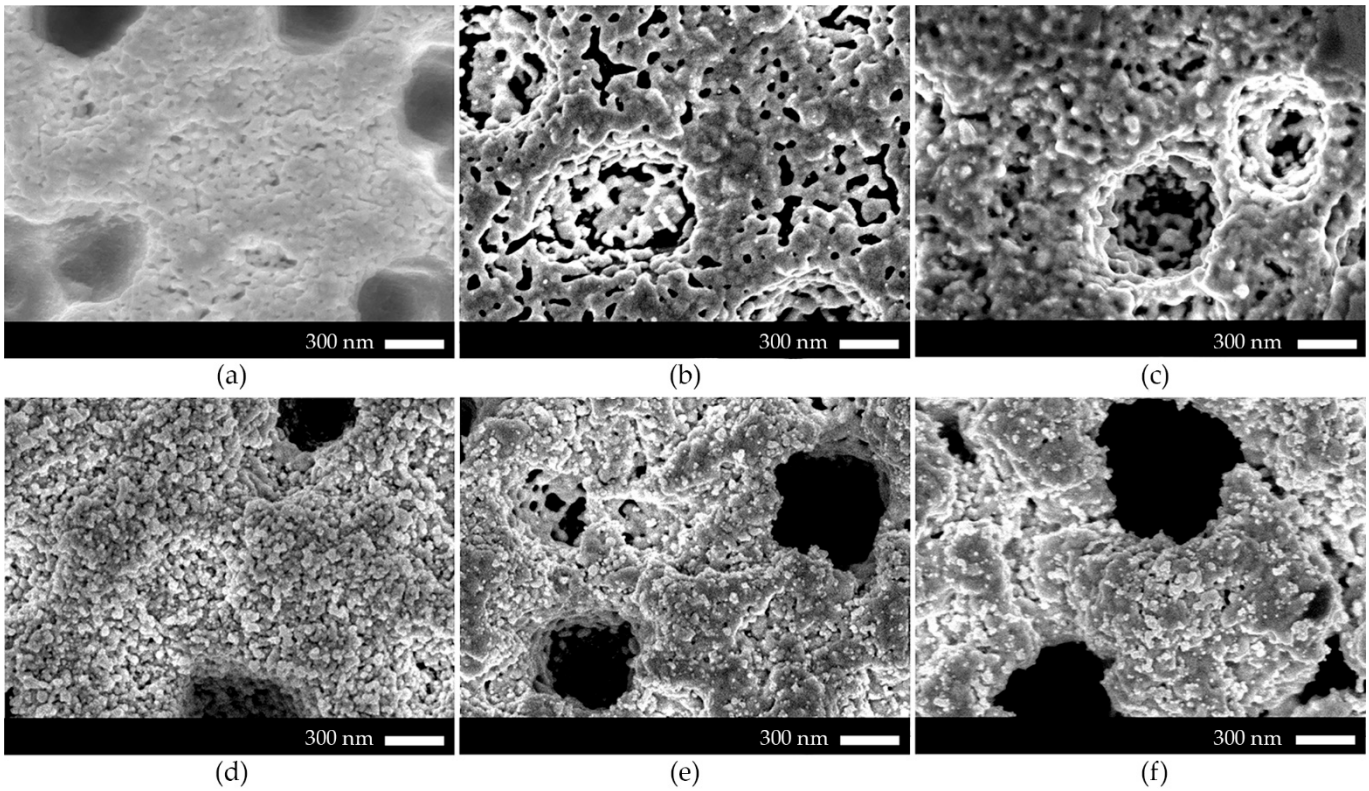

Figure 6. SEM images for the macro-PS after 30 min (**a**), 40 min (**b**), 50 min (**c**), 60 min (**d**), 70 min (**e**), and 80 min (**f**) of Au deposition.

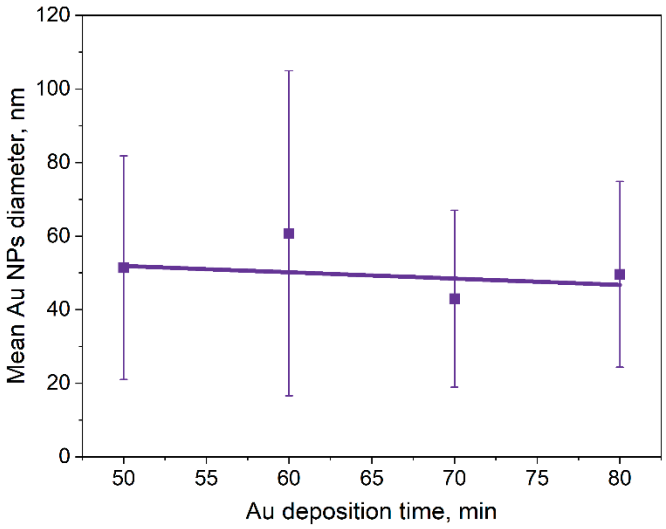

Figure 7. Mean Au NP diameter as a function of the gold deposition time on the macro-PS.

The observed kinetics of the Au film growth may be explained considering the presence of a thin microporous layer [58–60] over the entire macro-PS surface. This layer had a fractal-like geometry, which acted as the main source of the charge carriers for the redox reaction between the gold cations and the silicon wafer. This layer was also highly porous and composed of dense tiny voids. The growth of a continuous Au film on such a surface was even more confined by the voids compared with the meso-PS, leading to the formation of a dense Au NP layer in an early deposition stage (Figure 6a). As the redox reaction progressed with time, the thin microporous layer dissolved, leaving the bare macro-PS surface opened. At this growth stage, the number of Au seed nucleation centers increased, and the surface diffusion of gold atoms became possible. As the result, the Au NPs coalesced, and the quasicontinuous film was produced. For the rest of the deposition time, the gold layer grew similarly to the Au film on the meso-PS.

Figure 8 shows the XRD pattern for the Au-coated macro-PS after 50 min and 80 min of Au deposition. The patterns reported peaks associated with (111), (200), (220), and (311) Au crystal orientations, confirming the polycrystalline nature of the samples. Interestingly, in contrast to the XRD patterns for the Au-coated meso-PS (Figure 4a,b), no characteristic Si peak was observed in the XRD pattern for the gold-coated macro-PS, as shown in Figure 8a. This confirmed the introduced mechanism of Au film growth, where the coverage became uniform after the complete dissolution of the micro-PS layer. Apart from that, no noticeable difference between the Au-coated meso- and macro-PS samples was observed from the XRD; compare Figure 4a,b and Figure 8b.

We believe that the gold-coated macro-PS platform developed in this work can serve as an efficient nanoscale platform for SERS due to the strong plasmonic enhancement of the Raman signal. This can be better explained by closer inspection of the acquired SEM images in Figures 5 and 6. These images suggest that the obtained samples repeated the familiar nanoscale configuration, named metal nanovoids (NVs), which is one of the major candidates for mass utilization in SERS [61,62]. These NVs usually represent 500–2000 nm holes coated with various coinage metals and ensure the Raman signal enhancement by at least two basic optical effects: a localized plasmon mode with a strong rim component and multiple reflections of excitation light rays through the void. Moreover, the periodic morphology of the Me NVs guarantees a good spot-to-spot reproducibility of the SERS signal. The standard approach for Me NVs fabrication involves the deposition of a seed metallic layer, the coating with polymer spheres, the electrodeposition of a metal, and finally the dissolution of the polymer spheres. This procedure, however, is rather complex and limited by the small surface area covered with Me NVs. In contrast, our approach involved only two simple steps, electrochemical etching and chemical deposition, and can be extended up to wafer scale. It should be emphasized that the porosity and the thickness

of the macro-PS in this work were optimized to meet the dimensions of the standard Me NV configurations, while the optimum Raman signal enhancement was determined by the variation in the Au deposition time in the 30–80 min range.

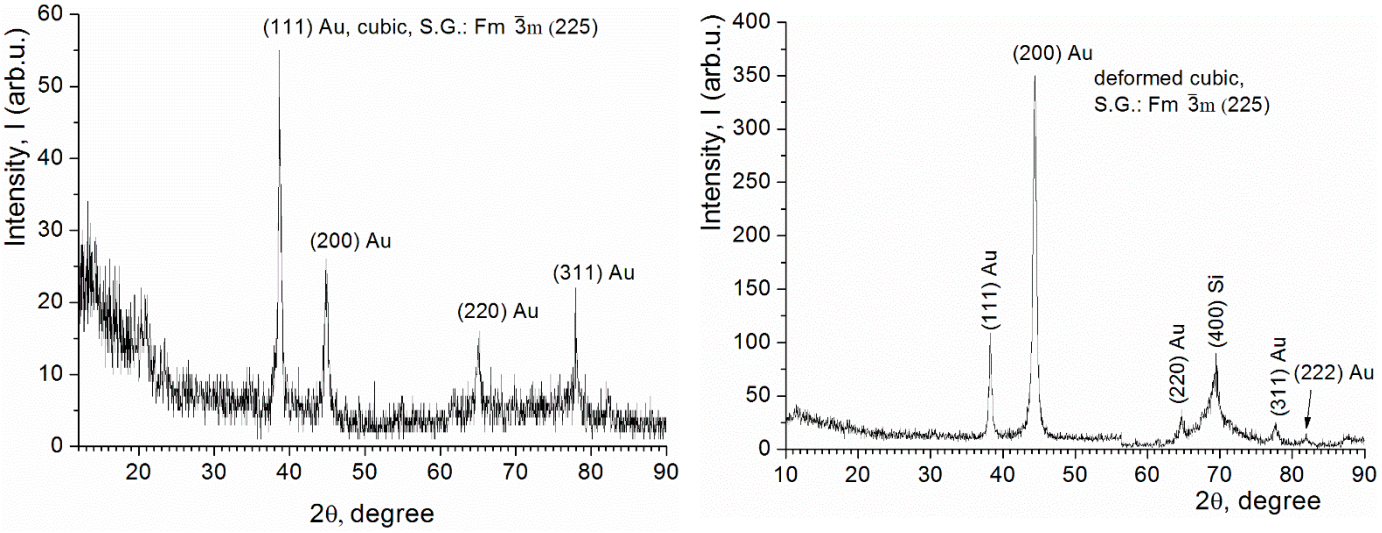

(**a**) (**b**)

Figure 8. XRD pattern for the macro-PS after 50 min (**a**) and 80 min (**b**) of Au deposition.

3.3. UV-Vis and SERS Measurements

Figure 9 depicts the reflectance spectra for the Au-coated meso-PS (Figure 9a) and macro-PS (Figure 9b) samples. These spectra clearly depict the reflectance minima around 480–495 nm for all samples, which could be associated with the (localized) surface plasmon resonance ((L)SPR). Considering that the highest Raman signal enhancement was achieved upon this (L)SPR condition, we therefore utilized the closest to this resonance and available for us laser wavelength of 532 nm. It should be emphasized that the (L)SPR observation for gold in the blue region of visible light is rather uncommon. It is known that isolated spherical Au nanoparticles demonstrate the LSPR band in the 520–580 nm wavelength region [63]. In some cases, however, it can shift towards the blue part of the spectrum, which is usually explained by the plasmons coupling between different nanoparticles upon shortening their spacing distance [64]. Therefore, our nanostructures were most likely to be affected by such a coupling effect, since they represented collections of densely packed Au nanoparticles comprising quasicontinuous films.

Figures 10 and 11 show the SERS spectra for 10^{-6} M R6G adsorbed on either the Au-coated meso- or macro-PS samples, respectively. To simplify the results representation and subsequent discussion, all the samples produced in this work and the corresponding fabrication regimes are summarized in Table 1. As can be seen from the figures, all SERS spectra exhibited the same characteristic Raman bands for R6G, namely 613 cm^{-1} (C-C-C ring in-plane bending); 772 cm^{-1} (C-H out of plane bending); 1185 cm^{-1} (C-H in-plane bending); 1311 cm^{-1} (C-O-C stretch); 1363 cm^{-1}, 1510 cm^{-1}, 1575 cm^{-1}, and 1650 cm^{-1} (aromatic C–C stretch). These results are in good agreement with the data reported elsewhere [65]. Figure 10 indicates that the intensity of the R6G SERS spectrum obtained for the best Au-coated macro-PS (sample 6) was two times higher than for the best Au-coated meso-PS (sample 2′, Figure 9). This confirms the stronger Raman signal enhancement provided by a configuration mimicking metal NVs compared with the usual metal NPs. The variation in the SERS spectra intensity between different nanostructures prepared on the same type of PS may be explained in terms of the stage of Au film growth. For example, the weak intensity of the R6G SERS spectra corresponded to the samples with a (quasi)continuous Au film (samples 2 and 5 in Figures 9 and 10, respectively; their morphology is highlighted in Figures 2a and 6b, respectively), while stronger SERS signals

originated from the Au NPs (samples 2′ and 6 in Figure 9, respectively; their morphology is highlighted in Figures 2c and 6c, respectively). These results can be correlated with the number of so-called "hot spots", tiny gaps in a metal nanostructure where the localization of a giant electromagnetic field occurred. The number of these spots was greater for the nanostructures exhibiting nanoscale roughness compared with the smooth continuous surfaces, leading to a higher probability for a molecule to be located within it and contribute to the enhancement of Raman scattering. With only this in mind, the reasons for the weak SERS response for sample 4 (Figure 10) are rather unclear. One may expect comparable intensities of R6G SERS spectra for both samples 4 and 6 because of the similar nanostructure morphology (compare Figure 6a,c). However, the correct results interpretation also requires a particle size comparison. The calculated average particle diameter for sample 6 was 51 nm ± 30 nm, which was close to the optimum diameter of 60 nm for an isolated Au NP, demonstrating the maximum SERS enhancement [66,67]. On the other hand, the individual Au NPs for sample 4 could not be resolved from the SEM images, suggesting their sizes were far smaller than the known optimum. A similar analysis can be conducted for the other Au-coated samples prepared on the same type of PS matrixes. This means that the careful choice of the initial PS morphological parameters, as well as the Au deposition regimes, can help to obtain the optimum Au nanostructure with the corresponding NP size and spacing for maximum SERS enhancement.

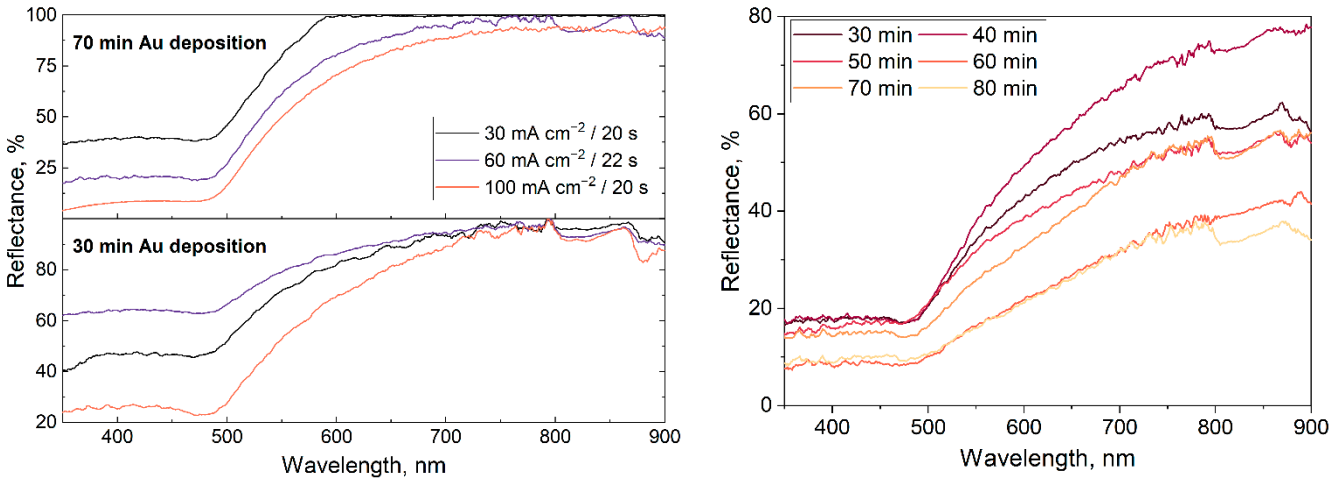

(**a**) (**b**)

Figure 9. Reflectance spectra for the meso-PS (**a**) and macro-PS (**b**) samples after Au deposition for different time periods.

Table 1. Fabrication regimes for the Au-coated meso- and macro-PS.

Sample	Etching Current Density for PS, mA cm^{-2}	Etching Time for PS, s	Au Deposition Time, min
1/1′	30	20	30/70
2/2′	60	22	30/70
3/3′	100	20	30/70
4	8	240	30
5	8	240	40
6	8	240	50
7	8	240	60
8	8	240	70
9	8	240	80

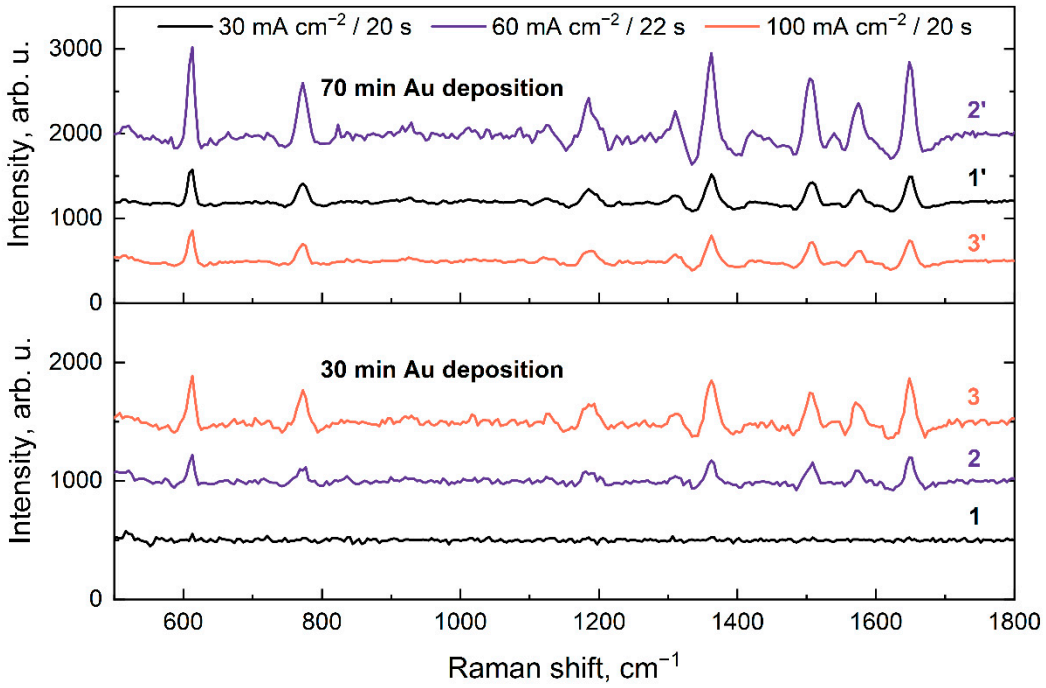

Figure 10. SERS spectra for 10^{-6} M R6G on the gold-coated meso-PS substrates.

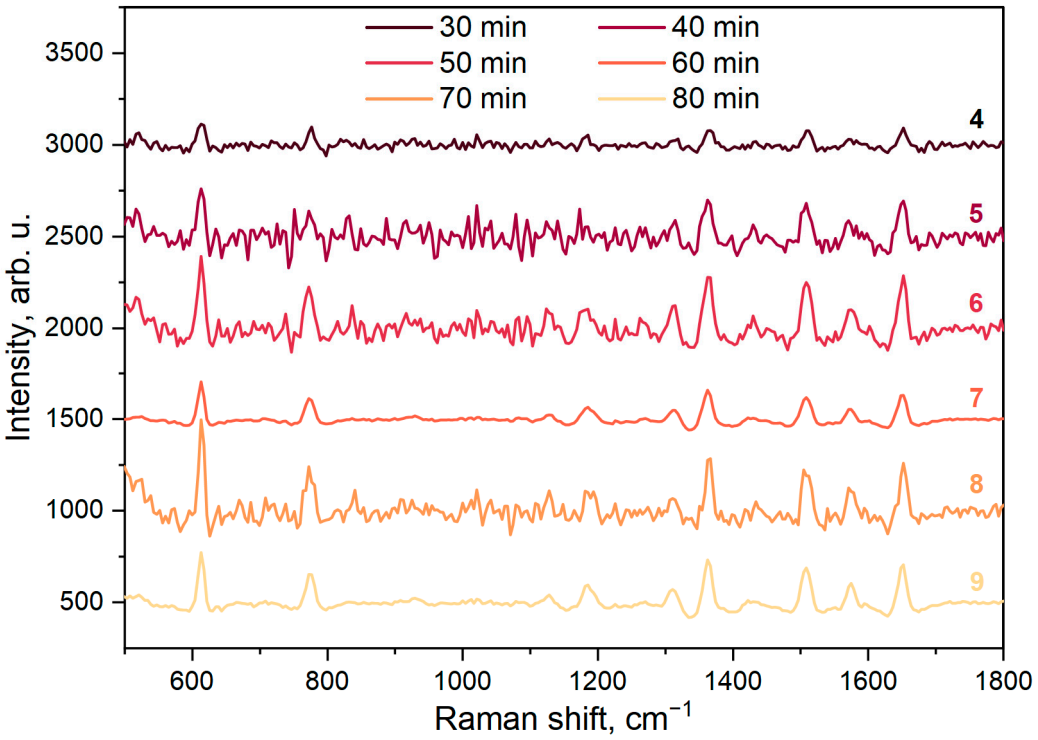

Figure 11. SERS spectra for 10^{-6} M R6G on the gold-coated macro-PS substrates.

4. Conclusions

In summary, we demonstrated that an effective SERS platform may be fabricated by Au electroless immersion deposition on meso- and macro-PS. SEM, XRD, and SERS analyses were carried out for sample characterization. In this work, a macro-PS template was fabricated to reproduce the Me NVs' structure [61,62], while the meso-PS matrixes were produced with three different porosities. SERS measurements were performed for the R6G molecules adsorbed on different Au-coated meso- and macro-PS samples at a

10^{-6} M concentration. It should be emphasized that the maximum SERS enhancement was achieved for the Me NVs' structures fabricated by a simple two-step procedure, while the current Me NVs' fabrication procedures involve at least four complex nanotechnology techniques, and the final structure is limited by a low surface area. We also demonstrated the correlation of the R6G SERS spectra intensity with the morphology and structural properties of Au coverage on the PS surface. Notably, the SERS response from the Au-coated PS samples may be tuned by the accurate choice of the initial PS morphological parameters, as well as the Au deposition regimes, which is explained by the formation of Au NPs with different sizes and spacings. Overall, both types of developed substrates demonstrated a sufficiently strong SERS response and show great promise for simple and versatile large-area plasmonic nanostructures fabrication.

Author Contributions: Author Contributions: conceptualization, S.Z., A.D., A.I.P. and H.B.; methodology, S.Z. and H.B.; software, S.Z.; validation, S.Z. and H.B.; formal analysis, S.Z.; investigation, S.Z. and A.C.; resources, H.B.; data curation, S.Z. and H.B.; writing—original draft preparation, S.Z.; writing—review and editing, S.Z., A.D., A.I.P. and H.B.; visualization, S.Z.; supervision, H.B.; project administration, H.B.; funding acquisition, H.B. All authors have read and agreed to the published version of the manuscript.

Funding: This research was funded by the Belarusian State Research Program "Photonics and Electronics for Innovations", tasks 1.8 (subprogram "Photonics and its application") and 2.2 (subprogram "Opto- and RF electronics"). Furthermore, S.Z., A.C. and H.B. thank the Russian Science Foundation (Project # 21-19-00761). In addition, the research of A.I.P. was partly supported by the RADON project (GA 872494) within the H2020-MSCA-RISE-2019 call and COST Action CA20129 "Multiscale Irradiation and Chemistry Driven Processes and Related Technologies" (MultIChem). A.I.P. thanks the Institute of Solid-State Physics, University of Latvia. ISSP UL as the Center of Excellence is supported through the Framework Program for European universities, Union Horizon 2020, H2020-WIDESPREAD-01–2016–2017-TeamingPhase2, under Grant Agreement No. 739508, CAMART2 project.

Data Availability Statement: The data presented in this study are available on request from the corresponding author.

Acknowledgments: The authors would like to thank Vitaly Bondarenko from the Belarusian State University of Informatics and Radioelectronics for the fruitful discussions on the mechanism of the gold coatings' formation on porous silicon.

Conflicts of Interest: The authors declare no conflict of interest.

References

1. Robertus, J. Principles of Protein X-Ray Crystallography, 3rd Edition By Jan Drenth (University of Groningen, The Netherlands). With a Major Contribution from Jeroen Mester (University of Lübeck, Germany). Springer Science + Business Media LLC: New York. 2007. Xiv + 3. *J. Am. Chem. Soc.* **2007**, *129*, 5782–5783. [CrossRef]
2. Bax, A.D.; Grzesiek, S. Methodological Advances in Protein NMR. *Acc. of Chem. Res.* **1993**, *26*, 131–138. [CrossRef]
3. Cavanagh, J.W.; Fairbrother, A.; Palmer, N., III; Skelton, M.R. *Protein NMR Spectroscopy: Principles and Practice*, 2nd ed.; Elsevier: Amsterdam, The Netherlands, 2007.
4. Kelly, S.M.; Jess, T.J.; Price, N.C. How to Study Proteins by Circular Dichroism. *Biochim. Biophys. Acta (BBA)-Proteins Proteom.* **2005**, *1751*, 119–139. [CrossRef]
5. Whitmore, L.; Miles, A.J.; Mavridis, L.; Janes, R.W.; Wallace, B.A. PCDDB: New Developments at the Protein Circular Dichroism Data Bank. *Nucleic Acids Res.* **2017**, *45*, D303–D307. [CrossRef] [PubMed]
6. Amendola, V.; Pilot, R.; Frasconi, M.; Maragò, O.M.; Iatì, M.A. Surface Plasmon Resonance in Gold Nanoparticles: A Review. *J. Phys. Condens. Matter* **2017**, *29*, 203002. [CrossRef]
7. Lane, L.A.; Qian, X.; Nie, S. SERS Nanoparticles in Medicine: From Label-Free Detection to Spectroscopic Tagging. *Chem. Rev.* **2015**, *115*, 10489–10529. [CrossRef]
8. Kneipp, J.; Kneipp, H.; Kneipp, K. SERS—A Single-Molecule and Nanoscale Tool for Bioanalytics. *Chem. Soc. Rev.* **2008**, *37*, 1052–1060. [CrossRef]
9. Zavatski, S.; Khinevich, N.; Girel, K.; Redko, S.; Kovalchuk, N.; Komissarov, I.; Lukashevich, V.; Semak, I.; Mamatkulov, K.; Vorobyeva, M.; et al. Surface Enhanced Raman Spectroscopy of Lactoferrin Adsorbed on Silvered Porous Silicon Covered with Graphene. *Biosensors* **2019**, *9*, 34. [CrossRef]

10. Xie, X.; Pu, H.; Sun, D.W. Recent Advances in Nanofabrication Techniques for SERS Substrates and Their Applications in Food Safety Analysis. *Crit. Rev. Food Sci. Nutr.* **2018**, *58*, 2800–2813. [CrossRef]
11. Burtsev, V.; Erzina, M.; Guselnikova, O.; Miliutina, E.; Kalachyova, Y.; Svorcik, V.; Lyutakov, O. Detection of Trace Amounts of Insoluble Pharmaceuticals in Water by Extraction and SERS Measurements in a Microfluidic Flow Regime. *Analyst* **2021**, *146*, 3686–3696. [CrossRef]
12. Cailletaud, J.; De Bleye, C.; Dumont, E.; Sacré, P.Y.; Netchacovitch, L.; Gut, Y.; Boiret, M.; Ginot, Y.M.; Hubert, P.; Ziemons, E. Critical Review of Surface-Enhanced Raman Spectroscopy Applications in the Pharmaceutical Field. *J. Pharm. Biomed. Anal.* **2018**, *147*, 458–472. [CrossRef] [PubMed]
13. Khinevich, N.; Zavatski, S.; Bandarenka, H.; Belyatsky, V.; Galyuk, E.; Ryneiskaya, O. Study of Diluted Meldonium Solutions by Surface Enhanced Raman Scattering Spectroscopy. *Int. J. Nanosci.* **2019**, *18*, 1940054. [CrossRef]
14. Khrustalev, V.V.; Khrustaleva, T.A.; Kahanouskaya, E.Y.; Rudnichenko, Y.A.; Bandarenka, H.V.; Arutyunyan, A.M.; Girel, K.V.; Khinevich, N.V.; Ksenofontov, A.L.; Kordyukova, L.V. The Alpha Helix 1 from the First Conserved Region of HIV1 Gp120 Is Reconstructed in the Short NQ21 Peptide. *Arch. Biochem. Biophys.* **2018**, *638*, 66–75. [CrossRef]
15. Kneipp, K.; Kneipp, H.; Bohr, H.G. Single-Molecule SERS Spectroscopy. In *Surface-Enhanced Raman Scatt*; Springer: Berlin/Heidelberg, Germany, 2006; pp. 261–277. [CrossRef]
16. Nie, S.; Emory, S.R. Probing Single Molecules and Single Nanoparticles by Surface-Enhanced Raman Scattering. *Science* **1997**, *275*, 1102–1106. [CrossRef] [PubMed]
17. Stiles, P.L.; Dieringer, J.A.; Shah, N.C.; Van Duyne, R.P. Surface-Enhanced Raman Spectroscopy. *Annu. Rev. Anal. Chem.* **2008**, *1*, 601–626. [CrossRef] [PubMed]
18. Langer, J.; Jimenez de Aberasturi, D.; Aizpurua, J.; Alvarez-Puebla, R.A.; Auguié, B.; Baumberg, J.J.; Bazan, G.C.; Bell, S.E.J.; Boisen, A.; Brolo, A.G. Present and Future of Surface-Enhanced Raman Scattering. *ACS Nano* **2019**, *14*, 28–117. [CrossRef] [PubMed]
19. Ding, S.-Y.; Yi, J.; Li, J.-F.; Ren, B.; Wu, D.-Y.; Panneerselvam, R.; Tian, Z.-Q. Nanostructure-Based Plasmon-Enhanced Raman Spectroscopy for Surface Analysis of Materials. *Nat. Rev. Mater.* **2016**, *1*, 16021. [CrossRef]
20. Natan, M.J. Concluding Remarks Surface Enhanced Raman Scattering. *Faraday Discuss.* **2006**, *132*, 321–328. [CrossRef]
21. Corni, S.; Tomasi, J. Surface Enhanced Raman Scattering from a Single Molecule Adsorbed on a Metal Particle Aggregate: A Theoretical Study. *J. Chem. Phys.* **2002**, *116*, 1156–1164. [CrossRef]
22. Mosier-Boss, P.A. Review of SERS Substrates for Chemical Sensing. *Nanomaterials* **2017**, *7*, 142. [CrossRef]
23. Poston, P.E.; Harris, J.M. Stable, Dispersible Surface-Enhanced Raman Scattering Substrate Capable of Detecting Molecules Bound to Silica-Immobilized Ligands. *Appl. Spectrosc.* **2010**, *64*, 1238–1243. [CrossRef] [PubMed]
24. Feng, L.; Xu, Y.-L.; Fegadolli, W.S.; Lu, M.-H.; Oliveira, J.E.B.; Almeida, V.R.; Chen, Y.-F.; Scherer, A. Experimental Demonstration of a Unidirectional Reflectionless Parity-Time Metamaterial at Optical Frequencies. *Nat. Mater.* **2013**, *12*, 108–113. [CrossRef]
25. Dubkov, S.V.; Savitskiy, A.I.; Trifonov, A.Y.; Yeritsyan, G.S.; Shaman, Y.P.; Kitsyuk, E.P.; Tarasov, A.; Shtyka, O.; Ciesielski, R.; Gromov, D.G. SERS in Red Spectrum Region through Array of Ag–Cu Composite Nanoparticles Formed by Vacuum-Thermal Evaporation. *Opt. Mater. X* **2020**, *7*, 100055. [CrossRef]
26. Kneipp, K.; Kneipp, H.; Manoharan, R.; Hanlon, E.B.; Itzkan, I.; Dasari, R.R.; Feld, M.S. Extremely Large Enhancement Factors in Surface-Enhanced Raman Scattering for Molecules on Colloidal Gold Clusters. *Appl. Spectrosc.* **1998**, *52*, 1493–1497. [CrossRef]
27. Jeon, T.Y.; Jeon, H.C.; Yang, S.-M.; Kim, S.-H. Hierarchical Nanostructures Created by Interference of High-Order Diffraction Beams. *J. Mater. Chem. C* **2016**, *4*, 1088–1095. [CrossRef]
28. Radu, A.I.; Ryabchykov, O.; Bocklitz, T.W.; Huebner, U.; Weber, K.; Cialla-May, D.; Popp, J. Toward Food Analytics: Fast Estimation of Lycopene and β-Carotene Content in Tomatoes Based on Surface Enhanced Raman Spectroscopy (SERS). *Analyst* **2016**, *141*, 4447–4455. [CrossRef]
29. Kim, S.; Zhang, W.; Cunningham, B.T. Coupling Discrete Metal Nanoparticles to Photonic Crystal Surface Resonant Modes and Application to Raman Spectroscopy. *Opt. Express* **2010**, *18*, 4300–4309. [CrossRef]
30. Gopalakrishnan, A.; Chirumamilla, M.; De Angelis, F.; Toma, A.; Zaccaria, R.P.; Krahne, R. Bimetallic 3D Nanostar Dimers in Ring Cavities: Recyclable and Robust Surface-Enhanced Raman Scattering Substrates for Signal Detection from Few Molecules. *ACS Nano* **2014**, *8*, 7986–7994. [CrossRef]
31. Yao, X.; Jiang, S.; Luo, S.; Liu, B.-W.; Huang, T.-X.; Hu, S.; Zhu, J.; Wang, X.; Ren, B. Uniform Periodic Bowtie SERS Substrate with Narrow Nanogaps Obtained by Monitored Pulsed Electrodeposition. *ACS Appl. Mater. Interfaces* **2020**, *12*, 36505–36512. [CrossRef]
32. Lazarouk, S.; Bondarenko, V.; Pershukevich, P.; La Monica, S.; Maiello, G.; Ferrari, A. Visible Electroluminescence from Al-Porous Silicon Reverse Bias Diodes Formed on the Base of Degenerate N-Type Silicon. *MRS Online Proc. Libr.* **1994**, *358*, 659. [CrossRef]
33. Bandarenka, H.; Redko, S.; Smirnov, A.; Panarin, A.; Terekhov, S.; Nenzi, P.; Balucani, M.; Bondarenko, V. Nanostructures Formed by Displacement of Porous Silicon with Copper: From Nanoparticles to Porous Membranes. *Nanoscale Res. Lett.* **2012**, *7*, 477. [CrossRef] [PubMed]
34. Bandarenka, H.V.; Khinevich, N.V.; Burko, A.A.; Redko, S.V.; Zavatski, S.A.; Shapel, U.A.; Mamatkulov, K.Z.; Vorobyeva, M.Y.; Arzumanyan, G.M. 3D Silver Dendrites for Single-Molecule Imaging by Surface-Enhanced Raman Spectroscopy. *ChemNanoMat* **2021**, *7*, 141–149. [CrossRef]

35. Korotcenkov, G. *Porous Silicon: From Formation to Application: Biomedical and Sensor Applications*; CRC Press: Boca Raton, FL, USA, 2016; Volume 2, ISBN 1482264579.
36. Bandarenka, H.V.; Girel, K.V.; Bondarenko, V.P.; Khodasevich, I.A.; Panarin, A.Y.; Terekhov, S.N. Formation Regularities of Plasmonic Silver Nanostructures on Porous Silicon for Effective Surface-Enhanced Raman Scattering. *Nanoscale Res. Lett.* **2016**, *11*, 262. [CrossRef] [PubMed]
37. Khajehpour, K.J.; Williams, T.; Bourgeois, L.; Adeloju, S. Gold Nanothorns–Macroporous Silicon Hybrid Structure: A Simple and Ultrasensitive Platform for SERS. *Chem. Commun.* **2012**, *48*, 5349–5351. [CrossRef] [PubMed]
38. Bandarenka, H.; Dolgiy, A.; Chubenko, E.; Redko, S.; Girel, K.; Prischepa, S.L.; Panarin, A.; Terekhov, S.; Pilipenko, V.; Bondarenko, V. Nanostructured Metal Films Formed onto Porous Silicon Template. *J. Nano Res. Trans. Tech. Publ.* **2016**, *39*, 235–255. [CrossRef]
39. Khinevich, N.; Bandarenka, H.; Zavatski, S.; Girel, K.; Tamulevičienė, A.; Tamulevičius, T.; Tamulevičius, S. Porous Silicon—A Versatile Platform for Mass-Production of Ultrasensitive SERS-Active Substrates. *Microporous Mesoporous Mater.* **2021**, *323*, 111204. [CrossRef]
40. Bandarenka, H.V.; Girel, K.V.; Zavatski, S.A.; Panarin, A.; Terekhov, S.N. Progress in the Development of SERS-Active Substrates Based on Metal-Coated Porous Silicon. *Materials.* **2018**, *11*, 852. [CrossRef]
41. Chernousova, S.; Epple, M. Silver as Antibacterial Agent: Ion, Nanoparticle, and Metal. *Angew. Chem.-Int. Ed.* **2013**, *52*, 1636–1653. [CrossRef]
42. Franci, G.; Falanga, A.; Galdiero, S.; Palomba, L.; Rai, M.; Morelli, G.; Galdiero, M. Silver Nanoparticles as Potential Antibacterial Agents. *Molecules* **2015**, *20*, 8856–8874. [CrossRef]
43. Dolgiy, A.; Redko, S.V.; Bandarenka, H.; Prischepa, S.L.; Yanushkevich, K.; Nenzi, P.; Balucani, M.; Bondarenko, V. Electrochemical Deposition and Characterization of Ni in Mesoporous Silicon. *J. Electrochem. Soc.* **2012**, *159*, D623. [CrossRef]
44. Magagnin, L.; Maboudian, R.; Carraro, C. Gold Deposition by Galvanic Displacement on Semiconductor Surfaces: Effect of Substrate on Adhesion. *J. Phys. Chem. B* **2002**, *106*, 401–407. [CrossRef]
45. Kong, L.; Dasgupta, B.; Ren, Y.; Mohseni, P.K.; Hong, M.; Li, X.; Chim, W.K.; Chiam, S.Y. Evidences for Redox Reaction Driven Charge Transfer and Mass Transport in Metal-Assisted Chemical Etching of Silicon. *Sci. Rep.* **2016**, *6*, 36582. [CrossRef]
46. Wang, C.H.; Sun, D.C.; Xia, X.H. One-Step Formation of Nanostructured Gold Layers via a Galvanic Exchange Reaction for Surface Enhancement Raman Scattering. *Nanotechnology* **2006**, *17*, 651–657. [CrossRef]
47. Grevtsov, N.; Burko, A.; Redko, S.; Khinevich, N.; Zavatski, S.; Niauzorau, S.; Bandarenka, H. Silicon Nanowire Arrays Coated with Ag and Au Dendrites for Surface-Enhanced Raman Scattering. *MRS Adv.* **2020**, *5*, 2023–2032. [CrossRef]
48. Merkus, H.G. *Particle Size Measurements*, 1st ed.; Springer: Dordrecht, The Netherlands, 2009; ISBN 1402090161.
49. Herino, R.; Bomchil, G.; Barla, K.; Bertrand, C.; Ginoux, J.L. Porosity and Pore Size Distributions of Porous Silicon Layers. *J. Electrochem. Soc.* **1987**, *134*, 1994. [CrossRef]
50. Smith, R.L.; Collins, S.D. Porous Silicon Formation Mechanisms. *J. Appl. Phys.* **1992**, *71*, R1–R22. [CrossRef]
51. Korotcenkov, G. *Porous Silicon: From Formation to Application: Formation and Properties*; CRC Press: Boca Raton, FL, USA, 2016; Volume 1, ISBN 1482264552.
52. Nativ-Roth, E.; Rechav, K.; Porat, Z. Deposition of Gold and Silver on Porous Silicon and inside the Pores. *Thin Solid Films* **2016**, *603*, 88–96. [CrossRef]
53. Panarin, A.Y.; Terekhov, S.N.; Kholostov, K.I.; Bondarenko, V.P. SERS-Active Substrates Based on n-Type Porous Silicon. *Appl. Surf. Sci.* **2010**, *256*, 6969–6976. [CrossRef]
54. Sing, K.S.W.; Everett, D.H.; Haul, R.A.W.; Moscou, L.; Pierotti, R.A.; Rouquerol, J.; Siemieniewska, T. Reporting Physisorption Data for Gas/Solid Systems with Special Reference to the Determination of Surface Area and Porosity (Recommendations 1984). *Pure Appl. Chem.* **1985**, *57*, 603–619. [CrossRef]
55. Venables, J. *Introduction to Surface and Thin Film Processes*; Cambridge University Press: Cambridge, UK, 2000; ISBN 0521785006.
56. Pimpinelli, A.; Villain, J. *Physics of Crystal Growth*; Cambridge University Press: Cambridge, UK, 1998; ISBN 0521551986.
57. Oura, K.; Lifshits, V.G.; Saranin, A.A.; Zotov, A.V.; Katayama, M. *Surface Science: An Introduction*; Springer: Berlin/Heidelberg, Germany, 2013; ISBN 3662051796.
58. Ponomarev, E.A.; Lévy-Clément, C. Macropore Formation on P-Type Si in Fluoride Containing Organic Electrolytes. *Electrochem. Solid State Lett.* **1998**, *1*, 42. [CrossRef]
59. Wehrspohn, R.B.; Chazalviel, J.; Ozanam, F. Macropore Formation in Highly Resistive P-Type Crystalline Silicon. *J. Electrochem. Soc.* **1998**, *145*, 2958. [CrossRef]
60. Cattarin, S.; Pantano, E.; Decker, F. Investigation by Electrochemical and Deflectometric Techniques of Silicon Dissolution and Passivation in Alkali. *Electrochem. Commun.* **1999**, *1*, 483–487. [CrossRef]
61. Cole, R.M.; Mahajan, S.; Bartlett, P.N.; Baumberg, J.J. Engineering SERS via Absorption Control in Novel Hybrid Ni/Au Nanovoids. *Opt. Express* **2009**, *17*, 13298–13308. [CrossRef] [PubMed]
62. Kelf, T.A.; Sugawara, Y.; Cole, R.M.; Baumberg, J.J.; Abdelsalam, M.E.; Cintra, S.; Mahajan, S.; Russell, A.E.; Bartlett, P.N. Localized and Delocalized Plasmons in Metallic Nanovoids. *Phys. Rev. B* **2006**, *74*, 245415. [CrossRef]
63. Haiss, W.; Thanh, N.T.K.; Aveyard, J.; Fernig, D.G. Determination of Size and Concentration of Gold Nanoparticles from UV-Vis Spectra. *Anal. Chem.* **2007**, *79*, 4215–4221. [CrossRef]

64. Han, X.; Liu, Y.; Yin, Y. Colorimetric Stress Memory Sensor Based on Disassembly of Gold Nanoparticle Chains. *Nano Lett.* **2014**, *14*, 2466–2470. [CrossRef]
65. Dieringer, J.A.; Wustholz, K.L.; Masiello, D.J.; Camden, J.P.; Kleinman, S.L.; Schatz, G.C.; Van Duyne, R.P. Surface-Enhanced Raman Excitation Spectroscopy of a Single Rhodamine 6G Molecule. *J. Am. Chem. Soc.* **2009**, *131*, 849–854. [CrossRef]
66. Zeman, E.J.; Schatz, G.C. An Accurate Electromagnetic Theory Study of Surface Enhancement Factors for Silver, Gold, Copper, Lithium, Sodium, Aluminum, Gallium, Indium, Zinc, and Cadmium. *J. Phys. Chem.* **1987**, *91*, 634–643. [CrossRef]
67. Krug, J.T.; Wang, G.D.; Emory, S.R.; Nie, S. Efficient Raman Enhancement and Intermittent Light Emission Observed in Single Gold Nanocrystals. *J. Am. Chem. Soc.* **1999**, *121*, 9208–9214. [CrossRef]